1	
2	
3	Assessing Free Tropospheric Quasi-Equilibrium for Different GCM
4	Resolutions Using a Cloud-Resolving Model Simulation of Tropical
5	Convection
6	
7	
8	
9	y w C I ZI
10 11	Xu Wang, Guang J. Zhang
12	Scripps Institution of Oceanography
13	La Jolla, CA 92093
14	24 volta, 0.17 2075
15	
16	E. Suhas
17	
18	Earth and Climate Science,
19	Indian Institute of Science Education and Research,
20	Pune, India
21	
22 23	
23 24	
25	
26	
27	
28	Submitted to Climate Dynamics
29	May 1, 2021
30	Revised: January 29, 2022
31	
32	
33	Corresponding author: Guang Zhang, Scripps Institution of Oceanography, La Jolla, CA
34	92093-0230, email: gzhang@ucsd.edu
35	

## 36 Abstract

37

38

39

40

41

42

43

44

45

46

47

48

49

50

51

52

53

54

5556

This study examines the free-tropospheric quasi-equilibrium at different global climate model (GCM) resolutions using the simulation of tropical convection by a cloud-resolving model during the Tropical Western Pacific International Cloud Experiment. The simulated dynamic and thermodynamic fields within the model domain are averaged over subdomains of different sizes equivalent to different GCM resolutions. These coarse-grained fields are then used to compute CAPE and its change with time, and their relationships with simulated convection. Results show that CAPE change with time is controlled predominantly by variations of thermodynamic properties in the planetary boundary layer for all subdomain sizes ranging from 64 km to 4 km. Lag correlation analysis shows that CAPE generation by the free-tropospheric dynamical advection (dCAPE<sub>ls</sub>) leads convective precipitation but is in phase with convective mass flux at 600 mb and 500 mb vertical velocity for all subdomain sizes. However, the correlation coefficients and regression slopes decrease as the subdomain size decreases for subdomain sizes smaller than 16 km. This is probably due to increased randomness of convection and more scale-dependence of the relationships when the subdomain size reaches the grey zone. By examining the sensitivity of the relationships of convection with dCAPE<sub>ls</sub> to temporal scales in different subdomain size, it shows that the quasi-equilibrium between dCAPE<sub>ls</sub> and convection holds well for timescales of 30 min or longer at all subdomain sizes. These results suggest that the free tropospheric quasiequilibrium assumption may still be useable even for GCM resolutions in the grey zone.

#### 1. Introduction

57

58

59

60

61

62

63

64

65

66

67

68

69

70

71

72

73

74

75

76

77

78

79

Convection occurs on spatial scales from sub-kilometer for shallow cumulus to tens of kilometers or larger for organized mesoscale convective systems. Despite its small scales, the role of deep convective towers in maintaining the atmospheric thermodynamic structure, atmospheric circulation and tropical energy balance was recognized more than half a century ago (Riehl and Malkus 1958; Manabe and Strickler 1964). Global climate models (GCMs) in the past and up till now typically have a horizontal grid spacing of ~100 km or larger. Within such a GCM grid box, the collective effect of convection is parameterized. In doing so, various assumptions were made to relate convection to grid-scale fields. Kuo (1965, 1974) proposed a moisture convergence closure, which related convection to column moisture convergence in the atmosphere. This closure was later modified by Tiedtke (1989) to determine cloud base updraft mass flux using moisture convergence in the subcloud layer. However, moisture convergence-based closure has been faulted for causing grid-point storms (Yano et al., 1998) and artificial CISK (conditional instability of the second kind) (Ooyama, 1982). Arakawa and Schubert (1974) proposed a convective quasiequilibrium, which assumed that the removal of convective instability by a population of convective clouds of different sizes within a GCM grid box equals the generation of convective instability by GCM-resolved processes. The convective quasi-equilibrium is probably the most fundamental assumption among many assumptions involved in convective parameterization schemes. From the tropical circulation point of view, Emanuel et al. (1994) showed that under the convective quasi-equilibrium framework the tropical atmospheric systems such as the Hadley circulation, tropical cyclones and Madden-Julian oscillation (MJO), are much easier to understand. The variation of the thickness of the convecting layer is entirely governed by the surface entropy fluxes into the atmosphere.

Other closures have also been proposed since then, including CAPE (convective available potential energy) relaxation-based closure (Fritsch and Chappell 1980; Kain and Fritsch 1993; Kain 2004; Zhang and McFarlane 1995), boundary layer turbulent kinetic energy (TKE) and convective inhibition (CIN)-based closure (Mapes 2000), boundary layer quasi-equilibrium closure (Raymond 1995), and free tropospheric quasi-equilibrium closure (Zhang 2002). Yano et al. (2013) provides a thorough review of different closure assumptions and their merits. CAPE is an approximation of cloud work function used in the Arakawa-Schubert (1974) convection scheme. It assumes that convective instability in the atmosphere is removed by convection within a relaxation time scale of a few hours. Based on the concept of activation control of convection by Mapes (1997), Mapes (2000) proposed a closure relating convection to boundary layer TKE and CIN. Fletcher and Bretherton (2010) and Hohenegger and Bretherton (2011) further tested it using a cloud-resolving model and single column model.

Zhang (2002) analyzed the observational data from the U.S. DOE Atmospheric Radiation Measurement (ARM) program and found that the net variation of convective instability as measured by CAPE is significant in both convective and non-convective situations. This variation is largely controlled by boundary layer temperature and moisture fluctuations. Further analyses of tropical and midlatitude observational data by Zhang (2003) and Donner and Phillips (2003) reached similar conclusions. This indicates that contributions to the *net* CAPE variation from temperature and moisture changes in the troposphere above the planetary boundary layer are insignificant. Based on this finding, Zhang (2002) proposed a free-tropospheric quasi-equilibrium (FTQE), in which CAPE generation by free-tropospheric large-scale processes is balanced by the removal of CAPE from convective heating. By design, a positive CAPE generation by the free

tropospheric large-scale processes was also used as a trigger condition<sup>1</sup> for convection onset. A similar trigger condition was used in Xie et al. (2004, 2019). An evaluation of trigger conditions in many convective parameterization schemes using observational data showed that this trigger condition is among the best performing trigger functions (Suhas and Zhang 2014). The application of the FTQE in the Zhang-McFarlane convection scheme (Zhang and McFarlane 1995) in the National Center for Atmospheric Research Community Atmosphere Model version 3 (NCAR CAM3), Community Climate System Model version 3 (CCSM3) and Community Earth System Model version 1 (CESM1) has shown improved simulations of some features of tropical convection, including MJO and intertropical convergence zone (ITCZ) (Zhang and Mu 2005a, b; Zhang and Wang 2006; Song and Zhang 2009; Zhang and Song 2010; Song and Zhang 2018). Wilcox and Donner (2007) implemented it into the Donner (1993) scheme in the Geophysical Fluid Dynamics Laboratory (GFDL) Atmospheric Model AM2. They showed, among other improvements, that the free tropospheric quasi-equilibrium closure greatly improved the simulation of the frequency of extreme precipitation events in the AM2. Benedict et al. (2013) showed that a version of the GFDL AM3 with the FTQE closure produced a better simulation of MJO than in the standard AM3 model. The FTQE closure was also implemented into the Finitevolume Atmospheric Model of IAP/LASG (FAMIL) GCM (Zhou et al. 2015) and tested in single column models of the NCAR CAM4 and CAM5 (Wang and Zhang 2013). Bechtold et al. (2014) incorporated this free-tropospheric quasi-equilibrium, with modifications to include some nonequilibrium elements from the planetary boundary layer, into the European Centre for Medium-

-

102

103

104

105

106

107

108

109

110

111

112

113

114

115

116

117

118

119

120

<sup>&</sup>lt;sup>1</sup> Here and in the rest of this paper trigger condition means a set of conditions that the atmospheric state or processes must satisfy before the call to convective parameterization is triggered.

range Weather Forecasts (ECMWF) Integrated Forecasting System (IFS) and showed that it improved the forecast of the diurnal variation of convection.

122

123

124

125

126

127

128

129

130

131

132

133

134

135

136

137

138

139

140

141

142

143

Both observational and GCM evaluations of FTQE are for GCM grid-spacings of ~200 km or larger. As GCM resolutions increase, is FTQE still a good assumption? Developing a convection scheme that can adapt to different GCM resolutions, i.e., scale-aware, has been an active research topic in recent years since Arakawa et al. (2011) proposed it (Arakawa and Wu 2013, Grell and Freitas 2014, Kwon et al. 2017). However, all these studies are concerned with how to factor in the fact that convective cloud fraction will no longer be negligible as GCM resolution increases to the grey zone (~10 km or less). Not as much has been explored on whether the closures of convective schemes are still useable as the GCM resolution approaches the grey zone. Suhas and Zhang (2015) evaluated several closure assumptions including CAPE-based, moisture convergence-based, and boundary layer turbulent kinetic energy (TKE)-based closures using a cloud-resolving model (CRM) simulation for different GCM resolutions. They found that the moisture convergence closure of Tiedtke (1989) is well correlated to convective precipitation and convective cloud mass flux at the 600 hPa level for a large range of grid spacings from 128 km to 4 km. To what extent is the FTQE assumption still applicable or appropriate for use in convective parameterization at high horizontal resolutions? We will address this issue in the paper.

At this point, it is necessary to clarify a nomenclature. In relating convection to large-scale fields through a closure, the large-scale fields are often referred to as "forcing", by which it implies a causality, that is, the large-scale forcing causes convection. Since the FTQE involves atmospheric circulation, it can be equally valid to argue that the large-scale circulation is a result of convection. More discussion on this will be presented in Section 3. In the paper, we will refrain

from using the word "forcing" to describe the circulation unless it is specified from observations to drive the CRM, in which case it is indeed used as forcing in the CRM setup.

The paper is organized as follows. In section 2, the CRM simulation data used for the evaluation will be described, along with a brief description of the free-tropospheric quasi-equilibrium and the analysis method. Section 3 will present the results. Section 4 will conclude the paper with a summary and some discussions.

### 2. Data and analysis method

The use of the cloud-resolving model (CRM) output for evaluating or developing convective parameterization schemes has been explored in the past (Xu et al. 1992; Plant and Craig 2008; Jones and Randall 2011). Although there are deficiencies in simulating the detailed structure of convective systems and the intensity of convective updrafts (Bryan et al. 2003; Varble et al. 2011), the macroscopic behavior of convection under a given large-scale condition is realistically simulated. Therefore, CRM data are still suitable for evaluating convective parameterization schemes.

The data used in this study are the same as those used in Suhas and Zhang (2015). They are from a CRM simulation of convection (Zeng et al. 2011) during the intensive observation period (IOP) of Department of Energy (DOE) Atmospheric Radiation Measurement (ARM) program's Tropical Warm Pool International Cloud Experiment (TWP-ICE) in Darwin Australia during the northern Australian summer monsoon season of 2006 (May et al. 2008). The model is the three-dimensional Goddard Cumulus Ensemble (GCE) model (Tao and Simpson 1993). It has 41 vertical levels from the surface to 21 km height, with a vertical resolution varying from 42.5 m at the bottom to 1 km at the top, and a horizontal resolution of 1 km. The simulation covers the monsoon break period from 2100 UTC 4 February 2006 to 2100 UTC 10 February 2006. The model domain

covers an area of 256 km  $\times$  256 km over the ARM Darwin site. The model simulation is output at 6-min interval.

To evaluate the free tropospheric quasi-equilibrium assumption for different subdomain sizes equivalent to various GCM resolutions, the raw data is averaged over different spatial and temporal scales. For spatial averaging, subdomain sizes of 64 km, 32 km, 16 km, 8 km and 4 km are used. Within each subdomain, we first identify convective grid points at the native CRM resolution of 1 km. A grid point is considered convective if its vertical velocity is greater than 1 m/s or less than -1 m/s and the sum of the mixing ratios of cloud liquid water and ice water exceeds  $1 \times 10^{-5}$  kg/kg. The GCM-equivalent domain-averaged convective mass flux ( $M_c = \sum_i \rho w/N$ ) is calculated to measure convective activity in each subdomain. Here w is vertical velocity at a CRM grid point, the summation is over all convective grid points within the subdomain, and N is the total number of CRM grid points for the subdomain. For convective precipitation, if a CRM column contains any convective grid point, then the surface precipitation is classified as convective, and the subdomain-mean convective precipitation is given by  $P_c = \sum_j P/N$ . Here the summation is over all convective columns. For temporal averaging, 1, 2, and 3 hours are chosen.

Before going into the details of methodology of evaluating the free tropospheric quasiequilibrium, we first define CAPE and its time rate of change resulting from subdomain-scale processes. CAPE is defined by the vertical integral of buoyancy of a parcel lifted from the most unstable level in the planetary boundary layer (PBL) to the level of neutral buoyancy:

$$CAPE = \int_{p_t}^{p_b} R_d (T_{pv} - \bar{T}_v) dlnp \quad (1)$$

where  $T_p(1 + 0.608q_p - q_l)$  and  $\overline{T}_v = \overline{T}(1 + 0.608\overline{q})$  are virtual temperatures of the air parcel and the domain average.  $p_b$  and  $p_t$  are pressure values at the parcel's originating level and the neutral buoyancy level, respectively.  $R_d$  is gas constant for dry air and  $q_l$  is liquid water condensed

following the reversible moist adiabat of the air parcel. Subscript *p* stands for parcel's properties and overbar for domain average. Thus, CAPE change with time can be rewritten as:

$$\frac{\partial CAPE}{\partial t} = \frac{\partial CAPE_p}{\partial t} + \frac{\partial CAPE_e}{\partial t} \quad (2)$$

where  $\frac{\partial CAPE_p}{\partial t} = R_d \frac{\partial}{\partial t} \int_{p_t}^{p_b} T_{pv} \, dlnp$  and  $\frac{\partial CAPE_e}{\partial t} = -R_d \frac{\partial}{\partial t} \int_{p_t}^{p_b} \bar{T}_v dlnp$  represent contributions to 193 194 CAPE change from changes of the parcel's thermodynamic properties and its environment in the 195 free troposphere, respectively. For an undiluted parcel, its virtual temperature is determined by the 196 temperature and moisture at its originating level in the PBL. With simple manipulation it can be shown (Zhang et al. 1998) that  $\frac{\partial CAPE_p}{\partial t}$  is related to surface entropy flux, and  $\frac{\partial CAPE_e}{\partial t}$  is the change 197 198 of the thickness of the convective layer. Using ARM observations, Zhang (2002, 2003) and Donner 199 and Phillips (2003) found that CAPE variation is largely controlled by boundary layer thermodynamic changes, that is,  $\frac{\partial CAPE}{\partial t} \approx \frac{\partial CAPE_p}{\partial t}$  and  $\frac{\partial CAPE_e}{\partial t} \approx 0$ . Based on this finding, Zhang 200 (2002) further decomposed  $\frac{\partial CAPE_e}{\partial t}$  into contributions from large-scale and convective scale 201 202 processes,

$$\frac{\partial CAPE_e}{\partial t} = \left(\frac{\partial CAPE_e}{\partial t}\right)_c + \left(\frac{\partial CAPE_e}{\partial t}\right)_{ls} \approx 0. (3)$$

This leads to the free tropospheric quasi-equilibrium assumption, which states that CAPE generation by large-scale advection in the free troposphere is in equilibrium with the CAPE removal by convective heating:

$$\left(\frac{\partial CAPE_e}{\partial t}\right)_c \approx -\left(\frac{\partial CAPE_e}{\partial t}\right)_{ls}. \tag{4}$$

This assumption was used to devise a closure to determine convective mass flux at the cloud base (Zhang, 2002; Zhang and Mu, 2005). In fact, the left-hand side of Eq. (4) is proportional to the cloud-based convective mass flux ( $M_b$ ):

where  $\eta$  is the net cloud mass flux normalized by the cloud base mass flux, i.e.,  $\eta = M_c/M_b$ . The 212 vertical integral on the rhs of Eq. (5) represents the consumption rate of CAPE per unit cloud-base 213

214 mass flux [see Eq. (8) of Zhang (2002)]. Thus,

221

225

226

231

$$M_b = \max\{-(\partial CAPE_e/\partial t)_{ls}, 0\}/F$$
 (6)

216 Here F denotes the vertical integration on the rhs of Eq. (5). Note that the diagnostic relationship 217 in Eq. (4) is well-known in large-scale tropical dynamics through scale analysis (e.g. Yano and 218 Bonazzola, 2009) and is the basis of weak temperature gradient approximation of tropical 219 circulation (Sobel et al., 2001). But it was not formally used in the context of convective 220 parameterization until Zhang (2002).

To evaluate the free tropospheric quasi-equilibrium closure for a given subdomain size 222 mimicking a corresponding GCM resolution, the following procedure is taken to calculate CAPE 223 changes due to subdomain-scale advection. First, CAPE is computed using Eq. (1) and subdomain-224 mean fields, and we call it CAPE<sub>0</sub>. Second, we compute advective tendencies of temperature  $(-\bar{v}\cdot$  $\nabla \bar{s} - \bar{\omega} \frac{\partial \bar{s}}{\partial p}$ ) and moisture  $(-\bar{v} \cdot \nabla \bar{q} - \bar{\omega} \frac{\partial \bar{q}}{\partial p})$  using subdomain-mean temperature, moisture and velocity fields from neighboring subdomains and finite difference as if they were representing 227 GCM grid point variables. Here s is dry static energy normalized by heat capacity of air, s = T + T $gz/c_p$ . The forcing from observations used to drive the CRM is also added uniformly to each 228 229 subdomain, as was done in the CRM simulation. These advective tendencies are then used to 230 update the subdomain-mean temperature and moisture fields at all levels above the parcel's originating level, so that the parcel's properties are not affected by this update:

232 
$$\bar{T}_1 = \bar{T}_0 + \left(-\bar{v} \cdot \nabla \bar{s} - \bar{\omega} \frac{\partial \bar{s}}{\partial p}\right) \Delta t + F_{advs} \Delta t \quad (7a)$$

233 
$$\bar{q}_1 = \bar{q}_0 + \left(-\bar{v} \cdot \nabla \bar{q} - \bar{\omega} \frac{\partial \bar{q}}{\partial p}\right) \Delta t + F_{advq} \Delta t \quad (7b)$$

where  $\Delta t$  is 6 minutes, the time interval for CRM model output, and  $\bar{T}_0$  and  $\bar{q}_0$  are temperature and moisture used to compute CAPE<sub>0</sub>.  $F_{advs}$  and  $F_{advq}$  are observed forcing of temperature and moisture that is used to drive the CRM. Next, CAPE is recomputed using Eq. (1) with the updated temperature  $\bar{T}_1$  and moisture  $\bar{q}_1$ , and we call it CAPE<sub>1</sub>. Thus, CAPE<sub>1</sub> is equivalent to CAPE in the atmosphere after the dynamics core but before convection parameterization is called in GCMs such as the NCAR CAM5. Finally, we obtain the CAPE change due to subdomain-scale (or GCM grid-scale) advection:

$$\left(\frac{\partial CAPE_e}{\partial t}\right)_{ls} = \frac{CAPE_1 - CAPE_0}{\Delta t} \tag{8}$$

Hereafter we will use the shorthand dCAPE<sub>Is</sub> for  $\left(\frac{\partial CAPE_e}{\partial t}\right)_{ls}$ . Note that neither  $\left(\frac{\partial CAPE_e}{\partial t}\right)_c$  nor  $\left(\frac{\partial CAPE_e}{\partial t}\right)_{ls}$  has contributions from changes of thermodynamic properties at and below the parcel's initiation level in boundary layer. Thus, this closure is decoupled from the surface and boundary layer processes that affect the convective parcel's properties. While this may seem unconventional since it is well known that convection is rooted in the boundary layer, it should be pointed out that heating and moistening, such as those from surface turbulent fluxes, in the boundary layer often do not directly affect deep convection. They first deepen the boundary layer, which subsequently leads to the development of shallow convection. Many previous observational and modeling studies have pointed out that shallow convection can serve to precondition the lower troposphere by moistening it (e.g. Kemball-Cook and Weare, 2001; Wu et al., 2009; Zhang and Klein, 2010) and can produce enhanced low-level mass convergence (Wu, 2003) before deep convection. The diabatic heating from shallow convection generates the grid-scale circulation which would

generate dCAPE<sub>ls</sub>. This dCAPE<sub>ls</sub> will lead to the development of deep convection if the environmental conditions are favorable for shallow to deep convection transition. In addition, although boundary layer forcing is not considered in the closure, a positive CAPE is required, which is largely controlled by the PBL properties. Therefore, deep convection is indirectly related to PBL properties in this closure.

### 3. Results

254

255

256

257

258

259

260

261

262

263

264

265

266

267

268

269

270

271

272

273

274

275

276

Fig. 1 shows the time series of observed precipitation during the IOP and dCAPE<sub>ls</sub> due to observed/background large-scale forcing applied to the CRM. Observationally, there is a close correspondence between variations of precipitation and dCAPE<sub>ls</sub>, with a correlation coefficient of 0.90 for points with positive dCAPE<sub>ls</sub>. Fig. 2 shows the time evolution of model precipitation and dCAPE<sub>ls</sub> for selected subdomain sizes (64 km and 32 km). Also shown are contributions to  $dCAPE_{ls}$  from the imposed observed forcing and advection from model generated circulations. For a 64 km subdomain, the total dCAPE<sub>ls</sub> largely comes from the contribution of model-generated circulations, and the prescribed, observed forcing is relatively small. As a result, the temporal variation of dCAPE<sub>ls</sub> is largely dominated by that of the contribution from model circulation, with a correlation coefficient of 0.92 between the two, and the correlation between the total dCAPE<sub>Is</sub> and the observed large-scale contribution is only 0.59. The precipitation variation clearly follows that of the total dCAPE<sub>ls</sub>. In a 32 km subdomain, dCAPE<sub>ls</sub> variation also predominantly comes from the model-generated contribution, with a correlation coefficient of 0.93. The contribution from the background forcing becomes much less significant, particularly during heavy precipitation events. The time series for other 64 km and 32 km subdomains are similar to those shown in the figure. This clearly demonstrates that the model-generated circulation on subdomain scale becomes more closely related to convection and the local relationship between convection

and circulation is less dependent on the imposed forcing for the CRM as the subdomain size decreases.

277

278

279

280

281

282

283

284

285

286

287

288

289

290

291

292

293

294

295

296

297

298

299

Zhang (2002, 2003) and Donner and Phillips (2003) showed using field observational data that on spatial scales of a few hundred kilometers, variability in CAPE is mainly controlled by planetary boundary layer variability in thermodynamic fields. In tropical atmosphere, this is at least partly due to the weak temperature gradients in the free troposphere. To examine if the CAPE variation is still controlled by the PBL properties as the spatial scale decreases, Fig. 3 shows the scatter plots of net CAPE change (dCAPE) versus contributions from boundary layer changes (dCAPE<sub>p</sub>), that is, the left-hand side vs. the first term on the right-hand side of Eq. (2), using 1hour average data. For all subdomain sizes, there is a strong correlation between dCAPE and dCAPE<sub>p</sub>, with correlation coefficients greater than 0.97. The slopes show that boundary layer contribution accounts for up to 93% of the total dCAPE. Furthermore, the relative contribution from the boundary layer increases as the domain size decreases. For example, at the 64 km subdomain size the regression slope is 0.938; it increases to 0.966 at 4 km subdomain size. These results, together with earlier observational results (Zhang 2002, 2003; Donner and Phillips 2003), indicate that boundary layer control of CAPE applies to all scales from ~100 km to grey zone scales of sub-10 km. In other words, Eq. (4) is a very good approximation to relate convection to GCM grid-scale CAPE generation in the free troposphere for all GCM grid spacings down to 4 km.

To verify this, Fig. 4 shows the relationship between dCAPE<sub>ls</sub> and convective mass flux at 600 mb. The red, cyan and orange lines are median values, first and third quartiles in each dCAPE<sub>ls</sub> bin, respectively. As in Suhas and Zhang (2015), the 600 mb convective mass flux is used to measure the amount of convection because it is difficult to define cloud base accurately in the

CRM. Convective mass flux increases linearly with dCAPE<sub>Is</sub> for 64 km, 32 km and 16 km, indicating GCM grid-scale advective CAPE generation, as represented by dCAPE<sub>Is</sub>, is closely related to convective mass flux at these subdomain sizes. The linear relationship between dCAPE<sub>Is</sub> and mass flux begins to degrade, with the median values plateauing off from the linear regression line, when the subdomain size further decreases to 8 km and 4 km, indicating that a larger amount of CAPE generation is needed to produce a given amount of convection as the GCM grid size decreases. The scatter is also increased. There are two possible explanations for the degeneration of the linear relationship at small subdomain sizes. First, as the subdomain size decreases, for a given grid-scale circulation and thermodynamic state, the stochastic behavior of convection becomes more prominent, thereby making convection in individual subdomains deviate more from the convective quasi-equilibrium. Second, as the subdomain size decreases, some of the convection may become GCM grid-resolved, resulting in less subgrid convective mass flux for given grid-scale state. This scale-aware issue should become more noticeable when the subdomain size becomes smaller.

To further evaluate the accuracy of free tropospheric quasi-equilibrium as GCM grid size decreases, Fig. 5 shows the lag correlation between dCAPE<sub>ls</sub> and convective precipitation, 600 mb convective mass flux, and 500 hPa vertical velocity, respectively, averaged over different subdomain sizes. The maximum correlation occurs when dCAPE<sub>ls</sub> leads convective precipitation. The lead time decreases from 18 minutes for 64 km subdomain size to 10 minutes for sub-10 km subdomain size. The maximum correlation coefficient remains about the same from 64 km subdomain sizes to 16 km subdomain sizes but decreases as the subdomain size further decreases. The variation of time lag with subdomain size can be explained by the strength of GCM grid-scale forcing and the time it takes for convection to adjust. Wang and Randall (1996) demonstrated that

it takes longer for convection to adjust under weak large-scale forcing, and vice versa. Fig. 4 shows that when the subdomain size is larger, the forcing is smaller. Thus, it takes longer for convective heating to adjust the atmosphere to an equilibrium state. The maximum correlation between convective mass flux and dCAPE<sub>ls</sub> occurs at zero lag for all subdomain sizes. This indicates that the development of convective precipitation lags convective updraft mass flux at 600 mb, the larger the subdomain, the longer the time lag. The fact that the highest correlation occurs between convective mass flux and dCAPE<sub>ls</sub> at zero lag suggests that using dCAPE<sub>ls</sub> as a closure to determine the amount of convection at a given GCM time step is reasonable. However, this should not be construed as a causal relationship, but rather a diagnostic one. In a balanced state it may be difficult or pointless to identify causality. In the past convection has been considered both as a cause and a result of large-scale circulation, depending on one's viewpoint. In dynamic models of tropical circulation (e.g. Gill 1980), the large-scale circulation is often viewed as a response to convective heating. On the other hand, in cloud-resolving models (e.g., Grabowski 2001) or singlecolumn models (Randall et al. 1996), large-scale forcing is prescribed to drive the models and convection in the models responds to the forcing. In the real world, large-scale circulation and convection interact with each other and neither view provides a complete picture of this interaction. In the context of convective parameterization, the amount of convection determined by a parameterization closure can be viewed as that needed to balance the model-predicted thermodynamic state or process, be it a cause or an effect. Therefore, it is unnecessary to determine whether one is the cause or the effect of the other.

323

324

325

326

327

328

329

330

331

332

333

334

335

336

337

338

339

340

341

342

343

344

345

Previous work by Davies et al. (2013) and Kumar et al. (2015) using Doppler radar observations of convection and ECMWF reanalysis data in Darwin, Australia found that convection is highly correlated with 500 mb large-scale vertical velocity. Another study by Qiao

and Liang (2016) used a regional climate model Climate-Weather Research and Forecasting (CWRF) to evaluate the effects of cumulus parameterization closures on summer precipitation simulation over the U.S. east coast and Gulf of Mexico. They showed that vertical velocity and moisture convergence-based closures reproduce the observed precipitation pattern and amount, and capture the frequency of heavy rainfall events better than CAPE-based closures. Since the large-scale generation of CAPE is closely linked to vertical velocity through vertical advection of dry static energy, this indirectly supports the free tropospheric quasi-equilibrium closure. As shown in Fig. 5c, the correlation coefficients reach a maximum at zero lag between dCAPE<sub>ls</sub> and 500 mb vertical velocity for all subdomain sizes, the same as that between dCAPE<sub>ls</sub> and convective updraft mass flux at 600 mb, indicating that dCAPE<sub>ls</sub>, 500 mb vertical velocity and convection occur concurrently. This concerted action between convection, adiabatic cooling and upward motion was noticed 30 years ago by Fraedrich and McBride (1989) as a free ride. It is also the basis of the weak temperature gradient approximation (Sobel et al. 2001). In terms of the values of correlation coefficients, dCAPE<sub>ls</sub> and 500 mb vertical velocity are highly correlated, with coefficients over 0.8 for all subdomain sizes. Nonetheless, it should be noted that dCAPE<sub>ls</sub> does not necessarily have a one-to-one relationship with the 500 mb vertical velocity since vertical motion at other levels also contributes to dCAPE<sub>ls</sub>. Fig. 6 shows the lag correlation between dCAPE<sub>ls</sub> and vertical velocity (color shading) at

346

347

348

349

350

351

352

353

354

355

356

357

358

359

360

361

362

363

364

365

366

367

368

Fig. 6 shows the lag correlation between dCAPE<sub>ls</sub> and vertical velocity (color shading) at different levels for different subdomain sizes. At zero lag, there is a broad maximum correlation in the mid-troposphere between 600 and 300 hPa. Also, there is a clear tilted structure, showing a time lag between the lower and upper troposphere for all subdomain sizes, with the lower tropospheric vertical velocity leading dCAPE<sub>ls</sub> and the upper tropospheric vertical velocity lagging dCAPE<sub>ls</sub>. The vertical velocity below 800 hPa leads dCAPE<sub>ls</sub> by as much as 2 hours for 64 km

subdomain size, reduced to less than half an hour for 4 km subdomain size. This indicates that the low-level grid-scale circulation acts first to generate dCAPE<sub>ls</sub>. Also shown in Fig. 6 is the time-lag correlation between convective mass flux and dCAPE<sub>ls</sub> (contours). Similar to vertical velocity, convective mass flux in the lower troposphere also leads dCAPE<sub>ls</sub>, although the vertical tilt in the time lag-height plot is not as much as that for vertical velocity. This suggests that vertical velocity below 800 hPa develops first, followed immediately by shallow convection, which reenforces the vertical motion. Then dCAPE<sub>ls</sub> peaks, accompanied by deep convection in the troposphere. This is consistent with previous observational and modeling studies that shallow convection often appears before deep convection (Wu 2003, Zhang and Klein 2010). The lead time decreases with subdomain size, reflecting that convection responds faster to stronger forcing as the subdomain size decreases.

From Figs. 5 and 6, convective mass flux and grid-scale vertical velocity w are closely related. Since  $\overline{w} = \frac{M_c}{\rho} + (1 - \sigma)\widetilde{w}$ , where  $\overline{w}$  is the subdomain-mean vertical velocity,  $M_c$  is convective mass flux,  $\rho$  is the air density,  $\sigma$  is the convective fraction and  $\widetilde{w}$  is vertical velocity in the convection-free environment within the subdomain, the difference between  $\overline{w}$  and  $M_c/\rho$  measures the compensating subsidence in the convection-free environment. Fig. 7 shows the vertical profiles of  $\overline{w}$  and  $M_c/\rho$  for different subdomain sizes. Convective mass flux exceeds  $\overline{w}$  at most levels except in the boundary layer, meaning that there is systematic compensating subsidence in the convective environment. The strength of the subsidence relative to convective mass flux or subdomain-mean vertical velocity decreases with subdomain size. In other words, more compensating subsidence occurs non-locally outside the subdomain where convection occurs as the subdomain size decrease. This is in agreement with the conceptual model of scale-dependence of convective effects as envisioned by Arakawa et al. (2011).

Fig. 8 shows the regression slope between 600 mb mass flux and dCAPE<sub>ls</sub> for different subdomain sizes. Similar to the correlation coefficients, for a given subdomain size the regression slope is the largest at zero lag. For different subdomain sizes, the regression slope first increases from 64 km subdomain sizes to 16 km subdomain sizes, but then decreases as the subdomain size becomes smaller, similar to that of correlation coefficient shown in Fig. 5b. However, the fluctuations are relatively smaller compared to the regression slopes themselves, in the range of 12 to 14 (kg m<sup>-2</sup> day<sup>-1</sup>)/(J kg<sup>-1</sup> hr<sup>-1</sup>). The slight decrease of the slopes for subdomain sizes  $\leq$  32 km can be explained by the following reasoning. Convection, as measured by precipitation or updraft mass flux, is positive-definite (i.e. the amount of convection cannot be negative) whereas the subdomain-scale dCAPE<sub>ls</sub> can be either positive or negative. In neighboring subdomains, dCAPE<sub>ls</sub> can be either positive or negative. In strongly positive dCAPE<sub>ls</sub> subdomains, it is likely there is active convection and convective precipitation. In negative dCAPE<sub>ls</sub> subdomains, there is likely no convection. Assume that there is a linear relationship between convection and dCAPE<sub>ls</sub> in subdomains where dCAPE<sub>ls</sub> is positive. When averaging over a larger subdomain containing subdomains with both positive and negative dCAPE<sub>ls</sub>, the rate of reduction of convective updraft mass flux will be smaller than the rate of reduction of dCAPE<sub>ls</sub> because the former contains positive or zero values only while the latter contains both positive and negative values. Thus, the ratio of convective mass flux to dCAPE<sub>ls</sub> for larger subdomains is larger than that for smaller subdomains, as seen in Fig. 8. A similar GCM-resolution dependence was also recognized by Xiao et al. (2015) and Yun et al. (2017) when examining the scale-awareness of vertical transport in the Zhang-McFarlane convection scheme.

392

393

394

395

396

397

398

399

400

401

402

403

404

405

406

407

408

409

410

411

412

413

414

Finally, to examine the sensitivity of the relationships between  $dCAPE_{ls}$  and convective mass flux to temporal scales for different subdomain sizes, Fig. 9 shows the variation of correlation

coefficients and regression slopes between dCAPE<sub>Is</sub> and 600 mb convective mass flux with time averaging intervals from 6 minutes to 3 hours for all subdomain sizes. The correlation coefficients for 32 km to 4 km subdomain sizes have a maximum at 30 min averaging time and then decrease slightly as the averaging intervals increase to 3 hours. For 64 km subdomain size, the correlation coefficient reaches a maximum at 1-hr averaging interval. However, its variation with averaging time intervals is relatively small. For the regression slopes, their variations with averaging time intervals have a similar pattern to that for the correlation coefficients. Therefore, these indicate that free tropospheric quasi-equilibrium between the subdomain scale forcing (i.e. dCAPE<sub>Is</sub>) and convection holds well for timescales of 30 min or longer, implying that for GCM applications with 30-min timestep, the free tropospheric quasi-equilibrium assumption is suitable.

### 4. Conclusions

This study uses the cloud-resolving model simulation of convection in Darwin, Australia to examine the validity of the free tropospheric quasi-equilibrium assumption for different spatial scales equivalent to GCM grid sizes from 64 km to 4 km. The CRM output is averaged over different subdomains equivalent to different GCM resolutions to investigate the relationships between convection, as measured by convective precipitation and convective mass flux at the 600 mb level, and the generation of convective available potential energy, dCAPE<sub>ls</sub>, by subdomain-scale circulation. Results show that although observed advective forcing is used to drive the CRM simulation of convection, CAPE generation for convection on subdomain scales is dominated by model-generated circulation when subdomain sizes become smaller. It is further shown that the total CAPE variation is controlled by contributions from the boundary layer properties on all spatial scales from 64 km down to 4 km subdomain sizes. The smaller the subdomain size, the larger the contribution from the boundary layer. For 64 km, the boundary layer contributes about

93% to the total CAPE variation. For sub-10 km (8 to 4 km) subdomain sizes, it contributes as much as 96% to the total CAPE variation. This implies that convective removal and large-scale generation of CAPE in the free troposphere are largely in balance, with their sum accounting for about less 7 to 4% of the total CAPE change (Fig. 3).

438

439

440

441

442

443

444

445

446

447

448

449

450

451

452

453

454

455

456

457

458

459

460

Convective precipitation, mass flux at 600 mb and vertical velocity at 500 mb all correlate well with dCAPE<sub>ls</sub> for subdomain sizes from 64 km to 4 km, suggesting that the free tropospheric quasi-equilibrium assumption can be applied to GCMs with resolutions in the grey zone. However, the correlation coefficient decreases as subdomain size decreases for subdomain sizes smaller than 16 km. This is likely due to increased randomness of convection and more noticeable scaledependence of the relationships when the subdomain size reaches the grey zone. The regression slope also becomes smaller with decreasing subdomain sizes on these scales, although the decrease is relatively small. This can be explained by the fact that convection is positive-definite whereas the free tropospheric forcing can be either positive or negative. Thus, as the subdomain size becomes smaller, the same amount of CAPE generation by the grid-scale circulation will correspond to a smaller amount of convection in the averaging domain. This implies that although free tropospheric quasi-equilibrium can still be useable as the GCM resolution increases, it needs to be modified to account for the decreasing regression slope in order to make it scale-aware. Finally, the sensitivity of relationship between dCAPE<sub>ls</sub> and convective mass flux at 600 mb to temporal scales for all subdomain sizes is examined. It shows that their correlations remain similar for all subdomain sizes for timescales of 30 min or longer. However, there is a noticeable increase for 8 km and 4 km subdomain sizes from 6 min to 30 min intervals. As for the regression slops, there is also little change for different averaging intervals for all subdomain sizes, especially timescales longer than 30 min. These results indicate that the free tropospheric quasi-equilibrium between dCAPE $_{ls}$  and convection holds well for 30 min or longer timescales at all subdomain sizes from 64 km to 4 km.

As the computing power increases, GCMs have begun to increase the horizontal resolution to 25 km or higher. This requires convective schemes to be able to adapt to the higher resolutions. While some schemes have incorporated the fact that convective cloud fraction within a GCM grid box typically increases with the GCM resolution, not much has been done to modify convection parameterization closure. This study provides a diagnostic evaluation on a closure assumption, which can be used to guide future development of a scale-aware closure for convection parameterization in high-resolution GCMs.

Acknowledgment: This material is based upon work supported by the Department of Energy, Office of Science, Biological and Environmental Research Program (BER) under Award Number DE-SC0022064 and by the NSF Grant AGS-2054697. Xu Wang is also supported by the National Natural Science Foundation of China (NSFC) under Award Number 41805069 and the Office of China Postdoctoral Council (OCPC) under Award Number 20190003. We would like to thank Dr. Xiping Zeng for making the cloud-resolving model simulation output available to us. The post-processed data used in this study and associated codes are provided through a public repository at http://doi.org/10.5281/zenodo.4542461.

- 480 References:
- 481 Arakawa, A., and W.H. Schubert (1974): Interaction of a cumulus cloud ensemble with the large-
- scale environment, Part 1, *J. Atmos. Sci.*, **31(3)**, 674–701.
- 483 Arakawa, A., and C. M. Wu (2013): A unified representation of deep moist convection in
- numerical modeling of the atmosphere. Part I. J. Atmos. Sci., 70, 1977–1992,
- 485 doi:10.1175/JAS-D-12-0330.1.
- 486 Arakawa, A., J. H. Jung, and C. M. Wu (2011): Toward unification of the multiscale modeling of
- 487 the atmosphere. Atmos. Chem. Phys., 11, 3731–3742, doi:10.5194/acp-11-3731-2011.
- 488 Bechtold P., N. Semane, P. Lopez, J.-P. Chaboureau, A. Beljaars, and N. Bormann (2014):
- Representing equilibrium and non-equilibrium convection in large-scale models, *J. Atmos.*
- 490 *Sci.*, DOI: http://dx.doi.org/10.1175/JAS-D-13-0163.1.
- 491 Benedict, J. J., A. H. Sobel, E. D. Maloney, D. M. Frierson, and L. J. Donner (2013): Tropical
- intraseasonal variability in Version 3 of the GFDL Atmosphere Model, J. Clim., 26,
- 493 426-499.
- Bryan, G. H., J. C. Wyngaard, and J. M. Fritsch (2003): Resolution requirement for the simulation
- 495 of deep moist convection, *Mon. Wea. Rev.*, **131**, 2772–2792.
- Davies, L., C. Jakob, P. May, V. V. Kumar, and S. Xie (2013): Relationships between the large-
- scale atmosphere and the small-scale convective state for Darwin, Australia, *J. Geophys.*
- 498 Res. Atmos., 118, 11,534–11,545, DOI:10.1002/jgrd.50645.
- 499 Donner, L. J. (1993): A cumulus parameterization including mass fluxes, vertical momentum
- dynamics, and mesoscale effects, *J. Atmos. Sci.*, **50**, 889-906.
- Donner, L. J. and V. T. Phillips (2003): Boundary layer control on convective available potential
- energy: implications for cumulus parameterization, J. Geophys. Res., 108, 4701,

503 DOI:10.1029/2003JD003773. 504 Emanuel, K. A., J. D. Neelin, and C. S. Bretherton (1994): On large-scale circulation in convective 505 atmospheres, Q. J. Roy. Meteorol. Soc., 120, 1111–1143. 506 Fletcher, J. K., and C. S. Bretherton (2010): Evaluating boundary-layer based mass flux closures 507 using cloud-resolving model simulations of deep convection, J. Atmos. Sci., 67, 2212–2225. 508 Fraedrich, K., and J. L. McBride (1989): The physical mechanism of CISK and the free-ride 509 Sci., 46, 2642-2648. balance, J. Atmos. DOI: https://doi.org/10.1175/1520-510 0469(1989)046<2642:TPMOCA>2.0.CO;2 511 Fritsch, J. M., and C. F. Chapell (1980): Numerical prediction of convectively driven mesoscale 512 pressure systems, Part 1: Convective parameterization, J. Atmos. Sci., 37,1722–1733. 513 Gill, A. E. (1980): Some simple solutions for heat-induced tropical circulation, *Quarterly Journal* 514 of the Royal Meteorological Society, 106(449), 447-462. 515 Grabowski, W. W. (2001): Coupling cloud processes with the large-scale dynamics using the 516 cloud-resolving convection parameterization (CRCP), J. Atmos. Sci., 58, 978-997. 517 Grell, G. A. and S. R. Freitas (2014): A scale and aerosol aware stochastic convective 518 parameterization for weather and air quality modeling. Atmos. Chem. Phys., 14, 5233— 519 5250, doi:10.5194/acp-14-5233-2014. 520 Hohenegger, C., and C. S. Bretherton (2011): Simulating deep convection with a shallow 521 convection scheme, Atmos. Chem. Phys., 11, 10389–10406. 522 Jones, T. R., and D. A. Randall (2011): Quantifying the limits of convective parameterizations, J.

Geophys. Res., 116, D08210, DOI:10.1029/2010JD014913.

- Kain, J. S., and J. M. Fritsch (1993): Convective parameterization for mesoscale models: The
- Kain-Fritcsh scheme, The Representation of Cumulus Convection in Numerical Models,
- 526 *Meteorological Monographs*, **24**.
- Kain, J. S. (2004): The Kain-Fritsch convective parameterization: An update, J. Appl. Met., 43,
- 528 170-181.
- 529 Kemball-Cook, S. R., and B. C. Weare (2001): The onset of convection in the Madden-Julian
- 530 Oscillation, *J. Clim.*, **14**, 780-793.
- Kumar, V., C. Jacob, A. Protat, C. Williams, and P. May (2015): Mass-flux characteristics of
- tropical cumulus clouds from wind profiler observations at Darwin, Australia, *J. Atmos.*
- 533 *Sci.*, **72**, 1837–1855.
- Kuo H. L. (1965): On the formation and intensification of tropical cyclones through latent heat
- release by cumulus convection, *J. Atmos. Sci.*, **22**, 40–63.
- Kuo, H. L. (1974): Further studies of the parameterization of the influence of cumulus convection
- on large-scale flow, *J. Atmos. Sci.*, **31**, 1232–1240.
- Kwon, Y. C. and S.-Y. Hong (2017): A mass flux cumulus parameterization scheme across gray-
- zone resolutions, Mon. Wea. Rev., **145**, 583-598.
- Manabe, S., and R. F. Strickler (1964): Thermal equilibrium of the atmosphere with a convective
- 541 adjustment. J. Atmos. Sci., 21, 361–385.
- Mapes, B. (1997): Equilibrium vs. activation controls on large-scale variations of tropical deep
- convection. The Physics and Parameterization of Moist Atmospheric Convection, R. K.
- 544 Smith, Ed., Kluwer Academic Publishers, 321–358.
- Mapes, B. (2000): Convective inhibition, subgrid-scale triggering energy, and stratiform instability
- in a toy tropical wave model, *J. Atmos. Sci.*, **57**, 1515–1535.

547 May, P. T., J. H. Mather, G. Vaughan, K. N. Bower, C. Jakob, G. M. McFarquhar, G. G. Mace 548 (2008): The Tropical Warm Pool International Cloud Experiment, Bull. Amer. Meteor. Soc., 549 **89**, 629–645. 550 Ooyama, K. V. (1982): Conceptual evolution of the theory and modeling of the tropical cyclone, 551 J. Meteor. Soc. Jpn., **60**, 369-380. 552 Plant, R. S., and G. C. Craig (2008): A stochastic parameterization for deep convection based on 553 equilibrium statistics, J. Atmos. Sci., 65(1), 87–105. 554 Qiao, F., and X.-Z. Liang (2016): Effects of cumulus parameterization closures on simulations of 555 summer precipitation over the United States coastal oceans, J. Adv. Model. Earth Syst., 8, 556 764-785, doi:10.1002/2015MS000621. 557 Randall, D. A., K.-M. Xu, R. J. C. Somerville, and S. Iacobellis (1996): Single-column models 558 and cloud ensemble models as links between observations and climate models. J. Climate, 559 **9**, 1683-1697. 560 Raymond, D. (1995): Regulation of moist convection over the West Pacific warm pool, J. Atmos. 561 *Sci.*, **52(22)**, 3945–3959. 562 Riehl, H., and J. S. Malkus (1958): On the heat balance in the equatorial trough zone. *Geophysica*, 563 **6**, 503–538. 564 Sobel, A. H., Nilsson, J., and Polvani, L. M. (2001): The weak temperature gradient approximation 565 and balanced tropical moisture waves, J. Atmos. Sci., 58(23), 3650-3665. 566 Song, X., and G. J. Zhang (2009): Convection parameterization, tropical Pacific double ITCZ, and

25

upper ocean biases in the NCAR CCSM3. Part I: Climatology and atmospheric feedback,

567

568

*J. Climate*, **22**, 4299–4315.

- Song, X., and G. J. Zhang (2018): The roles of convection parameterization in the formation of
- double ITCZ syndrome in the NCAR CESM: I. Atmospheric processes. *Journal of*
- 571 Advances in modeling Earth Systems, 10(3), 842-866.
- 572 Suhas, E., and G. J. Zhang (2014): Evaluation of trigger functions for convective parameterization
- schemes using observations, *J. Climate*, **27**, 7647–7666, DOI: 10.1175/JCLI-D-13-
- 574 00718.1.
- 575 Suhas, E., and G. J. Zhang (2015): Evaluating convective parameterization closures using cloud-
- resolving model simulation of tropical deep convection, J. Geophys. Res. Atmos., 120,
- 577 DOI:10.1002/2014JD022246.
- Tao, W.-K., and J. Simpson (1993): The Goddard Cumulus Ensemble Model. Part I: Model
- description, Terr. Atmos. Oceanic Sci., 4, 19–54.
- Tiedtke, M. (1989): A comprehensive mass flux scheme for cumulus parameterization in large-
- 581 scale models, *Mon. Wea. Rev.*, **117**, 1779–1800.
- Varble, A., A. M. Fridlind, E. J. Zipser, A.S. Ackerman, J-P Chaboureau, J. Fan, A. Hill, S.A.
- MacFarlane, J-P Pinty and B. Shipway (2011): Evaluation of cloud-resolving model
- intercomparison simulations using TWP-ICE observations: Precipitation and cloud
- structure, *J. Geophys. Res.*, **116**, D12206, DOI:10.1029/2010JD015180.
- Wang, J., and D. A. Randall (1996): A cumulus parameterization based on the generalized
- convective available potential energy, *J. Atmos. Sci.*, **53**, 716–727.
- Wang, X., and M. Zhang (2013): An analysis of parameterization interactions and sensitivity of
- single-column model simulations to convection schemes in CAM4 and CAM5, *J. Geophys.*
- 590 Res., **118**, 8869–8880, DOI:10.1002/jgrd.50690.
- Wilcox, E. M., and L. J. Donner (2007): The frequency of extreme rain events in satellite rain-rate

- estimates and an atmospheric general circulation model, *J. Climate*, **20**, 53–69.
- 593 Wu, Z. (2003): A shallow CISK, deep equilibrium mechanism for the interaction between large-
- scale convection and large-scale circulations in the tropics, *J. Atmos. Sci.*, **60**, 377-392.
- Wu, C., B. Stevens, and A. Arakawa (2009): What controls the transition from shallow to deep
- 596 convection? *J. Atmos. Sci.*, **66**, 1793-1806.
- Xiao, H., W. I. Gustafson Jr., S. M. Hagos, C.-M. Wu, and H. Wan (2015): Resolution-dependent
- behavior of subgrid-scale vertical transport in the Zhang-McFarlane convection
- 599 parameterization, *J. Adv. Model. Earth Syst.*, **07**, DOI:10.1002/2014MS000356.
- Xie, S., M. Zhang, J. S. Boyle, R. T. Cederwall, G. L. Potter, and W. Lin (2004): Impact of a revised
- convective triggering mechanism on Community Atmosphere Model, Version 2,
- simulations: Results from short-range weather forecasts, *J. Geophys. Res.*, **109**, D14102,
- 603 DOI:10.1029/2004JD004692.
- Kie, S., Y.C. Wang, W. Lin, H.-Y. Ma, Q. Tang, S. Tang, X. Zheng, J. C. Golaz, G. J. Zhang, and
- M. Zhang (2019): Improved diurnal cycle of precipitation in E3SM with a revised
- convective triggering function. J. Adv. Mod. Earth. Syst., 11, 2290-2310,
- 607 https://doi.org/10.1029/2019MS001702
- 608 Xu, K. M., A. Arakawa, and S. K. Krueger (1992): The macroscopic behavior of cumulus
- ensembles simulated by a cumulus ensemble model, J. Atmos. Sci., 49, 2402-2420,
- 610 DOI:10.1175/1520-0469.
- Yano, J.-I., and Bonazzola, M. (2009): Scale analysis for large-scale tropical atmospheric
- dynamics, J. Atmos. Sci., **66(1)**, 159-172.
- Yano, J.-I., M. Bister, Z. Fuchs, L. Gerard, V.T.J. Philips, S.Barkidja, and J.-M. Piriou (2013):
- Phenomenology of convection-parameterization closure, Atmos. Chem. Phys., 12,

- 615 4111-4131.
- Yano, J.-I., Moncrieff, M. W., and McWilliams, J. C. (1998): Linear stability and single-column
- analyses of several cumulus parameterization categories in a shallow-water model, Q. J.
- 618 Roy. Meterol. Soc., **124**, 983-1005.
- 619 Yun, Y., J. Fan, H. Xiao, G. J. Zhang, S. J. Ghan, K.-M. Xu, P.-L. Ma, W. I. Gustafson, Jr., (2017):
- Assessing the resolution adaptivity of the Zhang-McFarlane cumulus parameterization
- with spatial and temporal averaging, J. Adv. Mod. Earth Sys., 9,
- 622 https://doi.org/10.1002/2017MS001035.
- Zeng, X., W.-K. Tao, T. Matsui, S. Xie, S. Lang, M. Zhang, D. Starr, and X. Li (2011): Estimating
- the Ice Crystal Enhancement Factor in the Tropics, *J. Atmos. Sci.*, **68**, 1424–1434.
- Zhang, G. J. (2002): Convective quasi-equilibrium in midlatitude continental environment and its
- effect on convective parameterization, J. Geophys. Res., 107(D14), 4220
- 627 DOI:10.1029/2001JD001005.
- Zhang, G. J. (2003): Convective quasi-equilibrium in the tropical western Pacific: Comparison
- with midlatitude continental environment, J. Geophys. Res., 108(D19), 4592,
- 630 DOI:10.1029/2003JD003520.
- Zhang, G. J., J. T. Kiehl, and P. J. Rasch (1998): Response of climate simulation to a new
- convective parameterization in the National Center for Atmospheric Research Community
- 633 Climate Model (CCM3), *J. Clim.*, 11, 2097-2115.
- 634 Zhang, G. J. and McFarlane, N.A. (1995): Sensitivity of climate simulations to the
- parameterization of cumulus convection in the Canadian Climate Centre general
- 636 circulation model. *Atmosphere-ocean*, **33(3)**, 407-446.

537	Zhang, G. J., and M. Mu (2005a): Simulation of the Madden-Julian oscillation in the NCAR CCM3
538	using a revised Zhang-McFarlane convection parameterization scheme, J. Clim., 18,
539	4049-4067.
540	Zhang, G. J., and M. Mu (2005b): Effects of modifications to the Zhang-McFarlane convection
541	parameterization on the simulation of the tropical precipitation in the National Center for
542	Atmospheric Research Community Climate Model, version 3. J. Geophys. Res., 110,
543	D09109, DOI:10.1029/2004JD005617.
544	Zhang, G. J., and X. Song (2010): Convection parameterization, tropical Pacific double ITCZ, and
545	upper ocean biases in the NCAR CCSM3. Part II: Coupled feedback and the role of ocean
546	heat transport, <i>J. Climate</i> , <b>23</b> , 800–812.
547	Zhang, G. J., and H. Wang (2006): Toward mitigating the double ITCZ problem in NCAR CCSM3
548	Geophys. Res. Lett., 33, L06709, DOI:10.1029/2005GL025229.
549	Zhang, Y., and Klein, S. A. (2010): Mechanisms affecting the transition from shallow to deep
550	convection over land: inferences from observations of the diurnal cycle collected at the
551	ARM Southern Great Plains site, J. Atmos. Sci., 67(9), 2943-2959.
552	Zhou, L., Q. Bao, Y. Liu, G. Wu, WC. Wang, X. Wang, B. He, H. Yu, and J. Li (2015): Global
553	energy and water balance: Characteristics from Finite- volume Atmospheric Model of the
554	IAP/ LASG (FAMIL1), J. Adv. Model. Earth Syst., 7, 1–20, DOI:10.1002/
555	2014MS000349.

# **Figure Captions:**

- Fig. 1: Time series of observed precipitation (mm/hr) and CAPE generation (J/kg/hr) by large-scale advective forcing averaged over the IOP domain during the break monsoon period (February 5 to February 10, 2006) of TWP-ICE IOP.
- Fig. 2: Sample time series of cloud-resolving model simulated precipitation (mm/hr) and net CAPE generation (J/kg/hr) in subdomains at size of (a) 64 km and (b) 32 km for 30 min time-averaging intervals. Contributions to net CAPE generation from observed forcing (black) and model-generated forcing (blue) are also shown to demonstrate their relative importance as subdomain size changes. The correlation coefficients between net CAPE generation and contribution from observed/model-generated forcing are given above each frame.
- Fig. 3: Scatter plots of total CAPE change (dCAPE/dt) versus CAPE change due to thermodynamic changes in the planetary boundary layer ( $dCAPE_p/dt$ ) for different subdomain sizes ranging from 64 km to 4 km. Each point represents a 1-hr average of model output at 6 min interval. The regression lines (black), slopes and correlation coefficients are also provided. For visual clarity, only a portion (chosen randomly) of data points is used in the scatterplots at 16, 8 and 4 km subdomain sizes, but all data are used in the calculation of statistics.
- Fig. 4: Scatter plots of convective mass flux at 600 mb and dCAPE<sub>ls</sub> for different subdomain sizes.

  The blue line is linear regression, with correlation coefficient and slope shown at the top of each plot. Red solid curves are for median values and green and yellow solid curves are for first and third quartiles, respectively. For plotting the quartile curves, the data are divided into a number of bins and the bin sizes are larger for smaller subdomains. For visual clarity, only a portion (chosen randomly) of data points is used in the scatterplots, but all

680	data are used in the calculation of statistics. Note that the horizontal and vertical scales are
681	different across the plots.
682	Fig. 5: Lag correlation (a) between dCAPE <sub>ls</sub> and convective precipitation, (b) between dCAPE <sub>ls</sub>
683	and convective mass flux at $600 \text{ mb}$ and (c) between dCAPE $_{ls}$ and $500 \text{ mb}$ vertical velocity
684	for subdomain sizes ranging from 64 km to 4 km. Positive values in x-axis mean dCAPE $_{\rm ls}$
685	leads the associated convective fields, and vice versa.
686	Fig. 6: Lag correlation between vertical velocity and dCAPE <sub>ls</sub> (color shading), and between
687	convective mass flux and dCAPE $_{ls}$ (contours) at (a) 64 km, (b) 32 km, (c) 16 km, (d) 8 km
688	and e) 4 km. Contour lines start at 0.2 with an interval of 0.2. Negative value in x-axis
689	means dCAPE <sub>ls</sub> lags vertical velocity and mass flux.
690	Fig. 7: Vertical profiles of subdomain-mean vertical velocity (W) and convective mass flux (MF)
691	for different subdomain sizes. MF is divided by air density $(\rho)$ at each level to give the
692	same unit as that for W.
693	Fig. 8: Regression slopes between $dCAPE_{ls}$ and $600$ mb convective mass flux at different time lags
694	for different subdomain sizes. Positive value in x-axis means dCAPE <sub>ls</sub> leads mass flux, and
695	vice versa.
696	Fig. 9: Lag 0 (a) correlation and (b) slope between dCAPE <sub>ls</sub> and 600 mb convective mass flux for
697	subdomain sizes ranging from 64 km to 4 km for different time-averaging intervals.
698	
699	

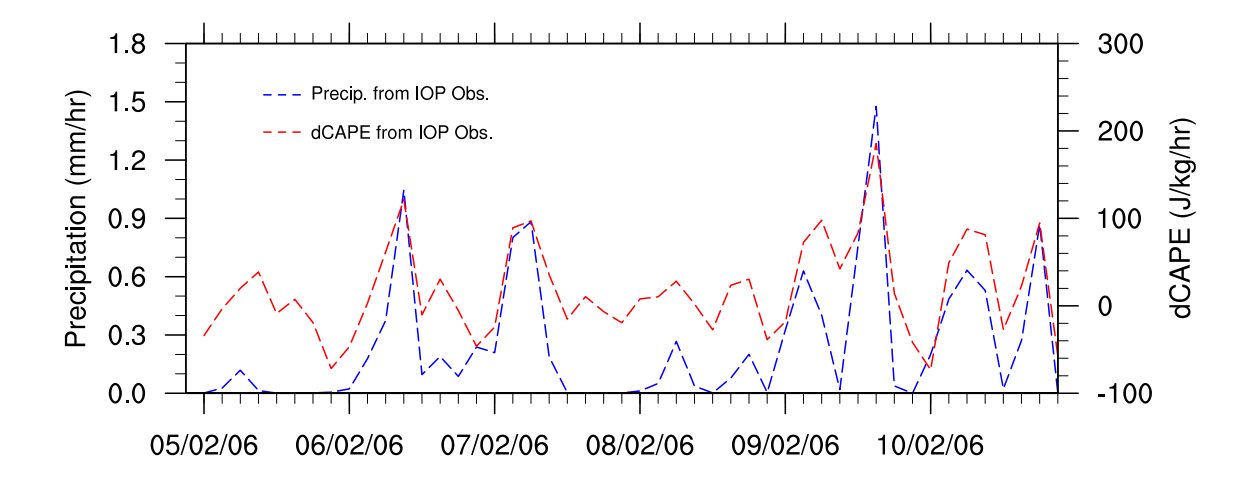


**Fig. 1** Time series of observed precipitation (mm/hr) and CAPE generation (J/kg/hr) by large-scale advective forcing averaged over the IOP domain during the break monsoon period (February 5 to February 10, 2006) of TWP-ICE IOP.



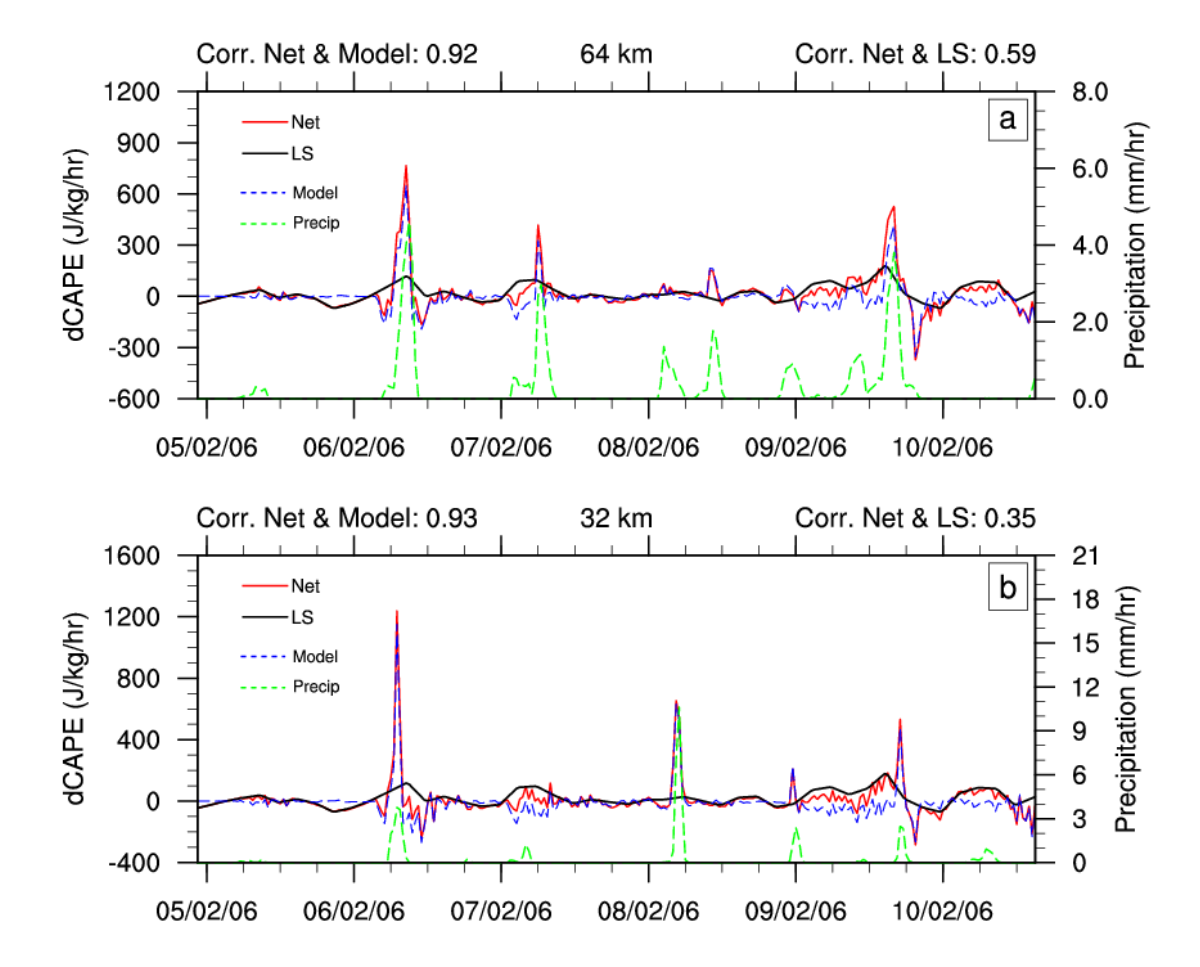


**Fig. 2** Sample time series of cloud-resolving model simulated precipitation (mm/hr) and net CAPE generation (J/kg/hr) in subdomains at size of (a) 64 km and (b) 32 km for 30 min time-averaging intervals. Contributions to net CAPE generation from observed forcing (black) and model-generated forcing (blue) are also shown to demonstrate their relative importance as subdomain size changes. The correlation coefficients between net CAPE generation and contribution from observed/model-generated forcing are given above each frame.

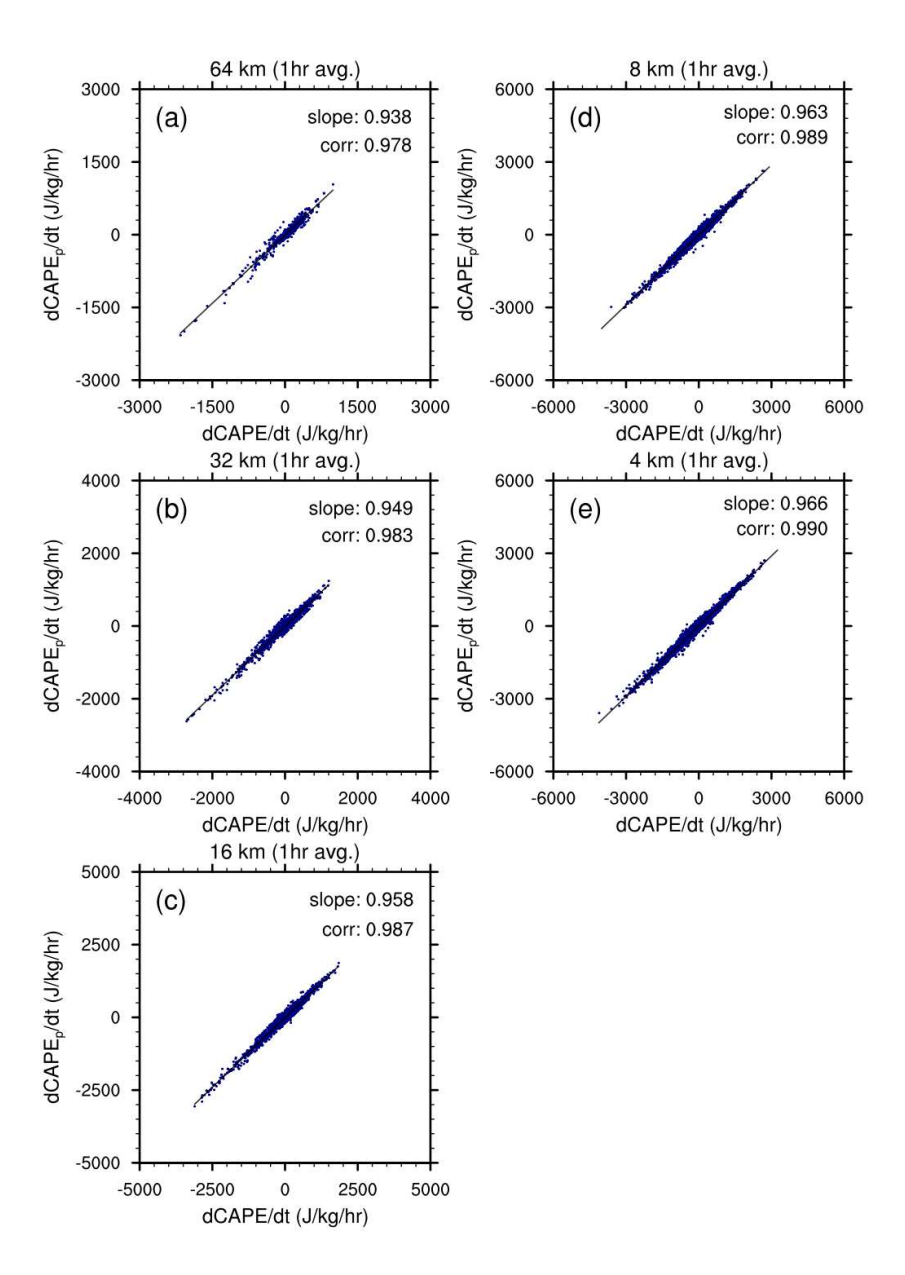


Fig. 3 Scatter plots of total CAPE change (dCAPE/dt) versus CAPE change due to thermodynamic changes in the planetary boundary layer ( $dCAPE_p/dt$ ) for different subdomain sizes ranging from 64 km to 4 km. Each point represents a 1-hr average of model output at 6 min interval. The regression lines (black), slopes and correlation coefficients are also provided. For visual clarity, only a portion (chosen randomly) of data points is used in the scatterplots at 16, 8 and 4 km subdomain sizes, but all data are used in the calculation of statistics.

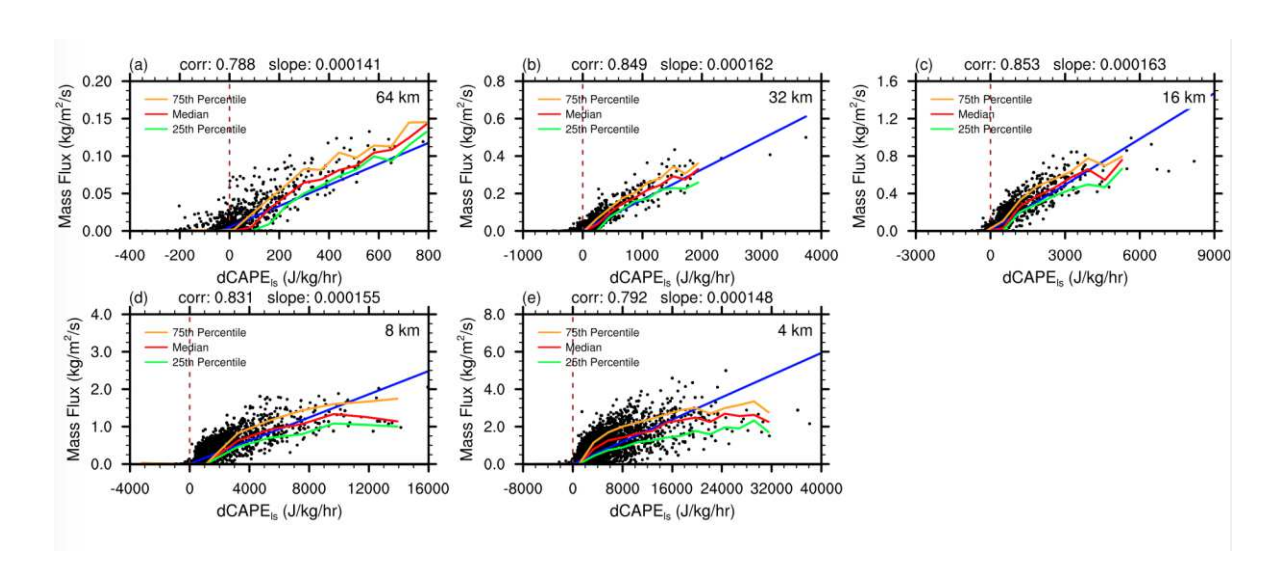
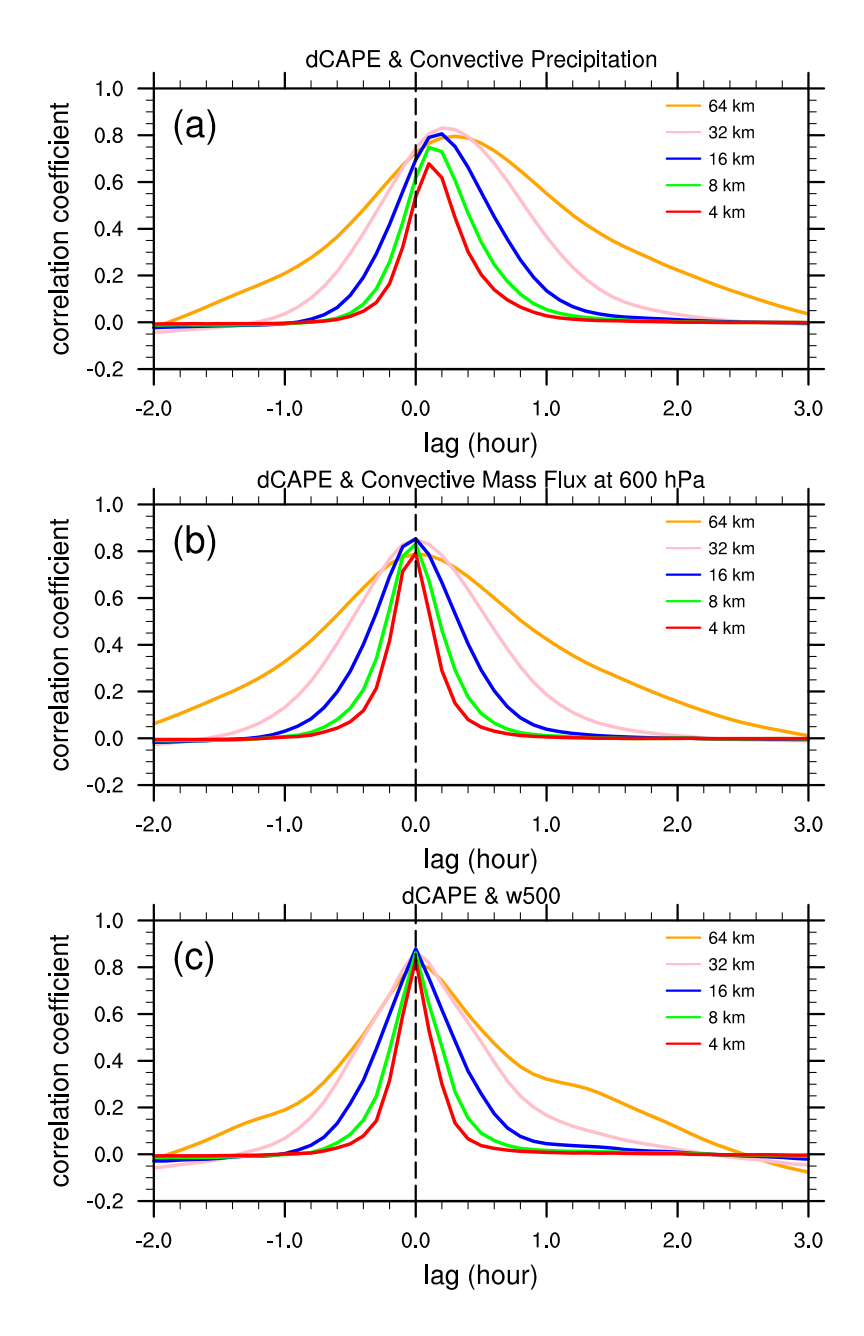
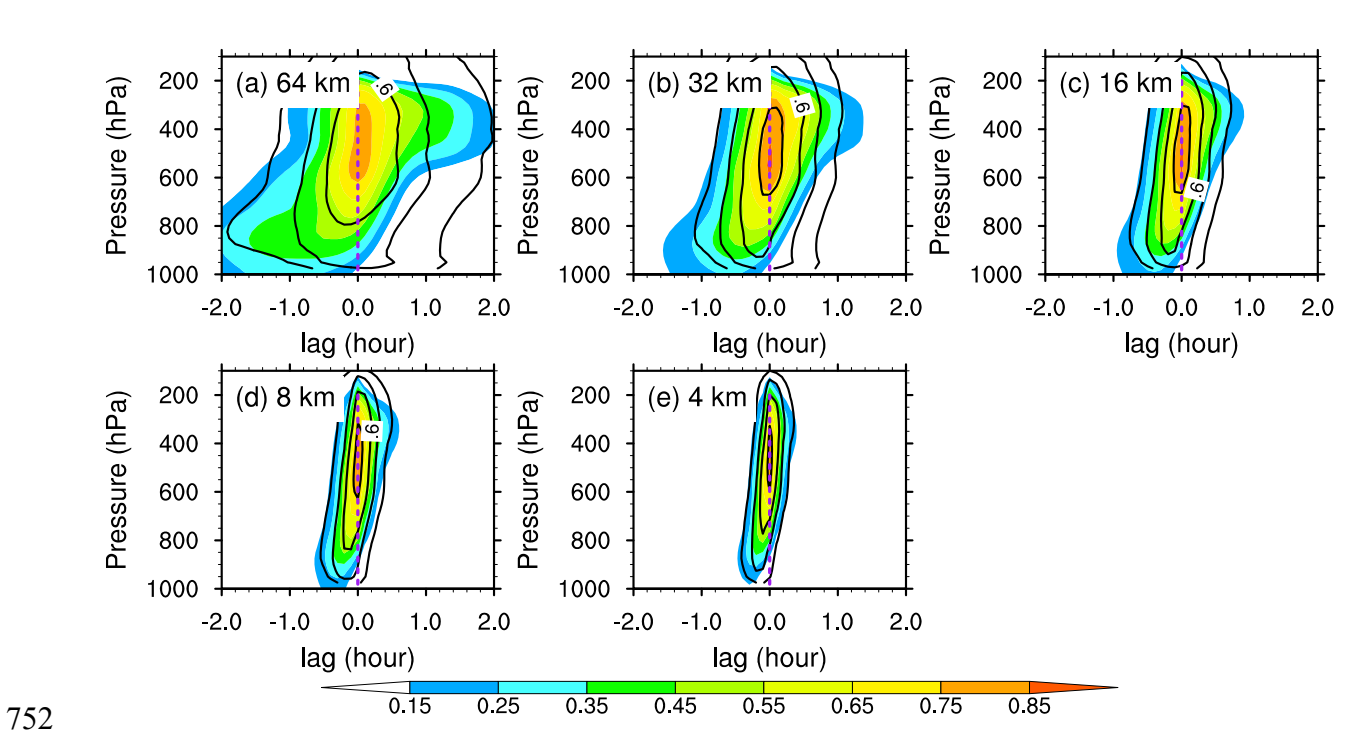


Fig. 4 Scatter plots of convective mass flux at 600 mb and dCAPE<sub>ls</sub> for different subdomain sizes. The blue line is linear regression, with correlation coefficient and slope shown at the top of each plot. Red solid curves are for median values and green and yellow solid curves are for first and third quartiles, respectively. For plotting the quartile curves, the data are divided into a number of bins and the bin sizes are larger for smaller subdomains. For visual clarity, only a portion (chosen randomly) of data points is used in the scatterplots, but all data are used in the calculation of statistics. Note that the horizontal and vertical scales are different across the plots.



**Fig. 5** Lag correlation (a) between dCAPE<sub>ls</sub> and convective precipitation, (b) between dCAPE<sub>ls</sub> and convective mass flux at 600 mb and (c) between dCAPE<sub>ls</sub> and 500 mb vertical velocity for subdomain sizes ranging from 64 km to 4 km. Positive values in x-axis mean dCAPE<sub>ls</sub> leads the associated convective fields, and vice versa.



**Fig. 6** Lag correlation between vertical velocity and dCAPE<sub>ls</sub> (color shading), and between convective mass flux and dCAPE<sub>ls</sub> (contours) at (a) 64 km, (b) 32 km, (c) 16 km, (d) 8 km and e) 4 km. Contour lines start at 0.2 with an interval of 0.2. Negative value in x-axis means dCAPE<sub>ls</sub> lags vertical velocity and mass flux.

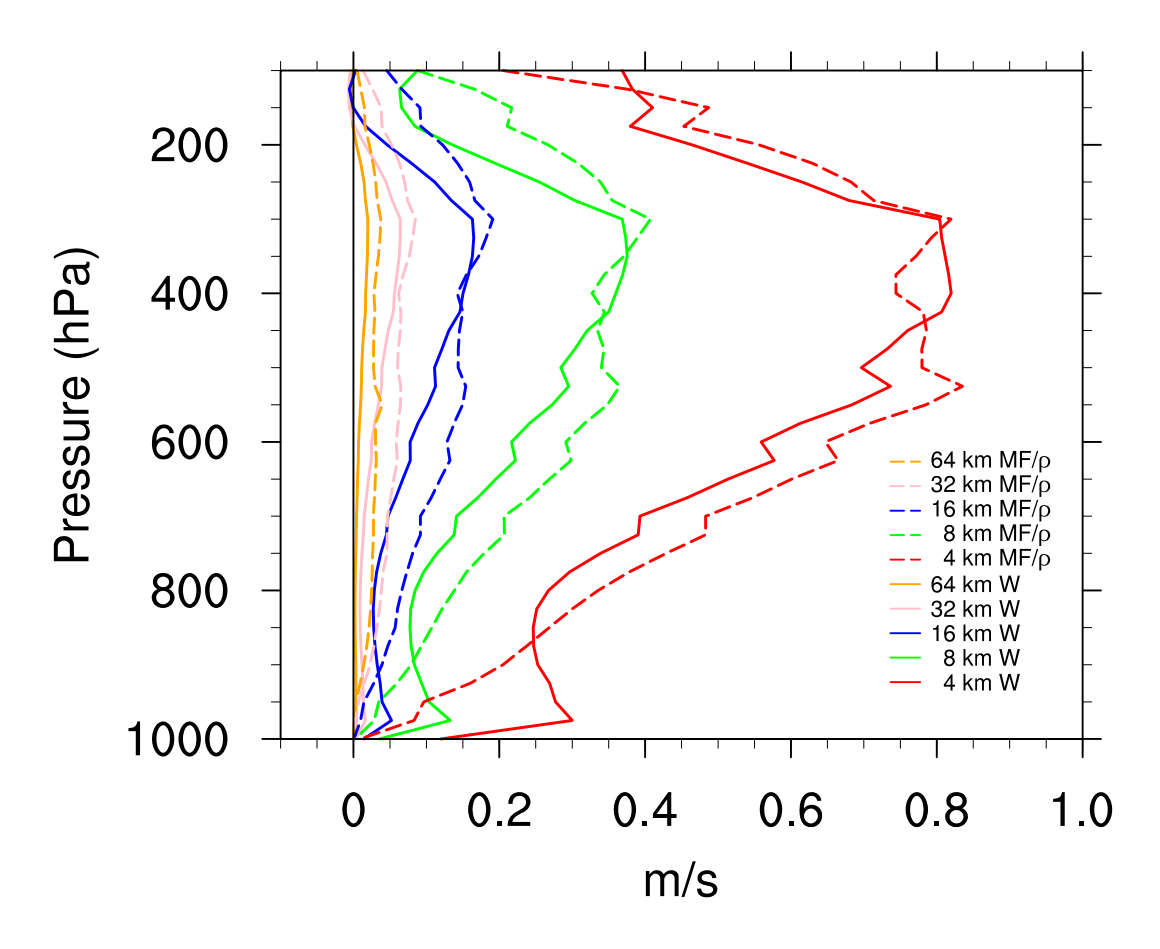


Fig. 7 Vertical profiles of subdomain-mean vertical velocity (W) and convective mass flux (MF) for different subdomain sizes. MF is divided by air density  $(\rho)$  at each level to give the same unit as that for W.

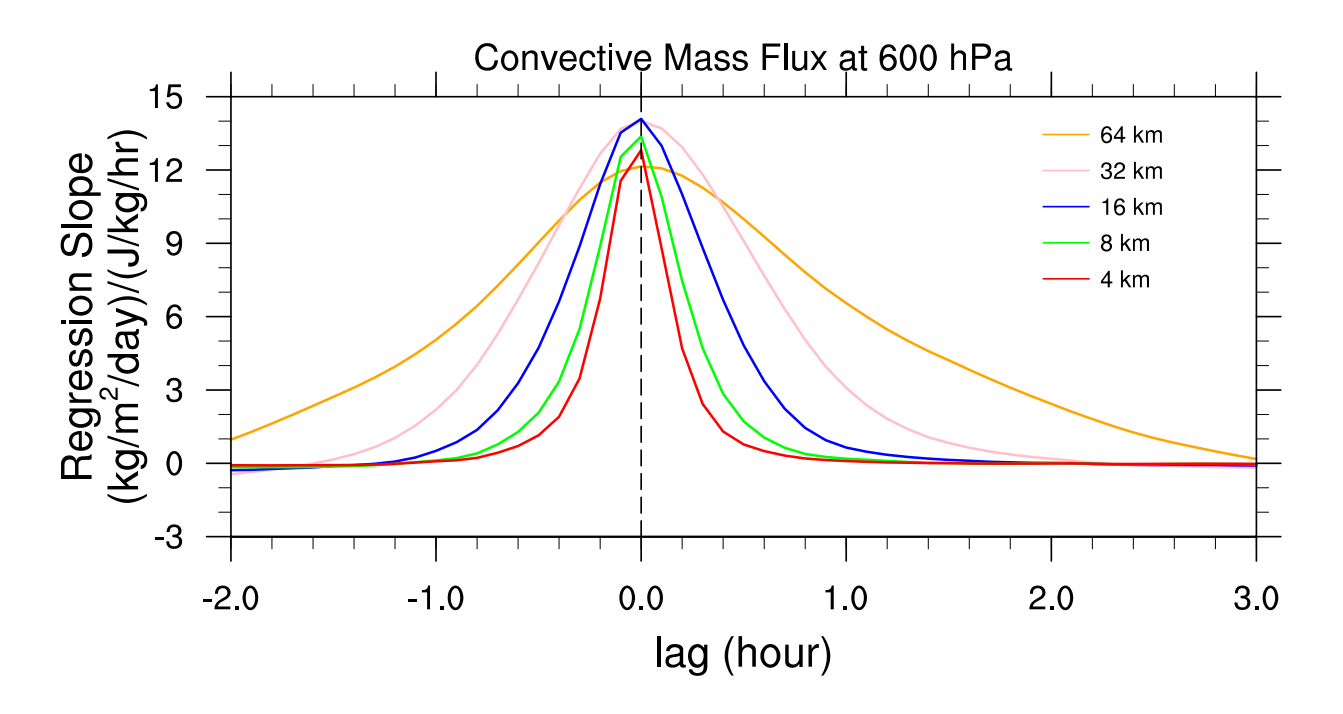


Fig. 8 Regression slopes between  $dCAPE_{ls}$  and 600 mb convective mass flux at different time lags for different subdomain sizes. Positive value in x-axis means  $dCAPE_{ls}$  leads mass flux, and vice versa.



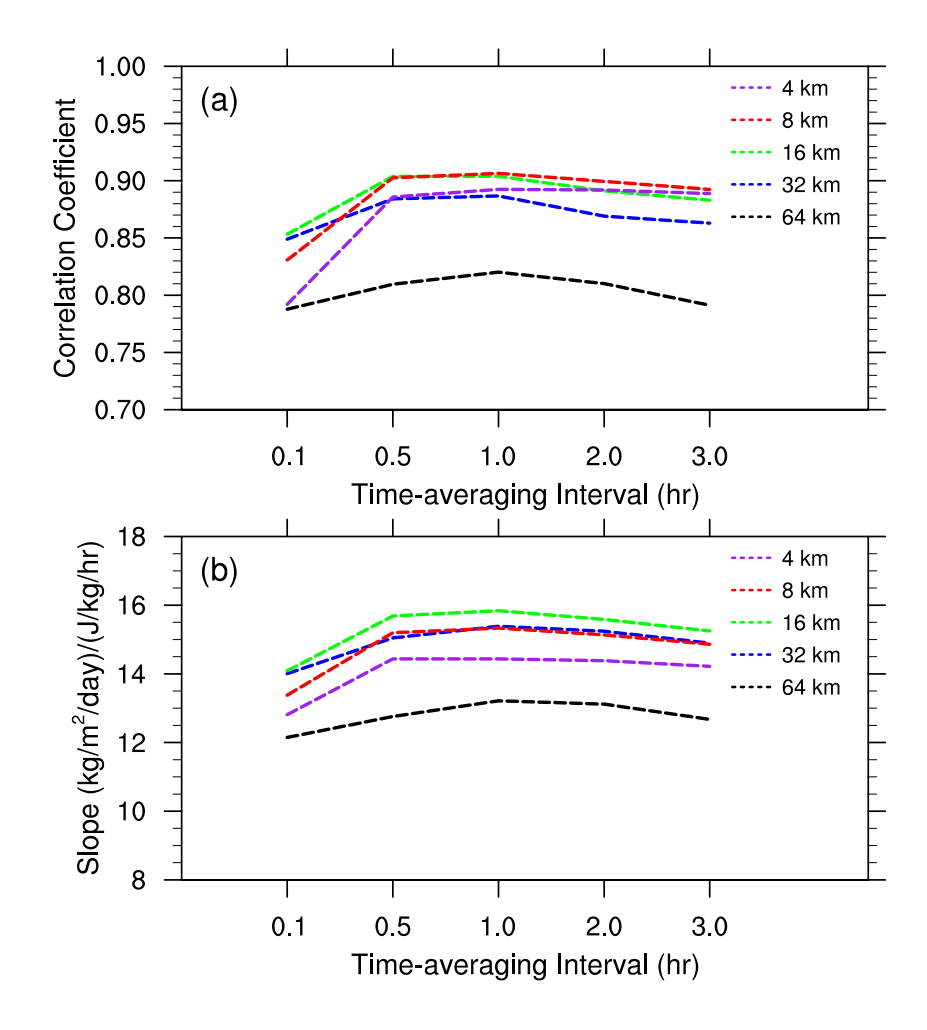


Fig. 9 Lag 0 (a) correlation and (b) slope between dCAPE $_{ls}$  and 600 mb convective mass flux for subdomain sizes ranging from 64 km to 4 km for different time-averaging intervals.